Redox reaction at buried ZnO/Ti thin film interface as seen by hard x-ray photoemission and thermal desorption spectroscopy

Ekaterina Chernysheva, Bertrand Philippe, Håkan Rensmo, Olof Karis, Roberto Felix Duarte, Mihaela Gorgoi, Sergey Grachev, Ekaterina Burov, Hervé Montigaud, Rémi Lazzari

Redox reaction at buried ZnO/Ti thin film interface as seen by hard x-ray photoemission and thermal desorption spectroscopy

Ekaterina Chernysheva [1,2], Bertrand Philippe [3], Håkan Rensmo [3], Olof Karis [3], Roberto Felix Duarte[4], Mihaela Gorgoi [4], Sergey Grachev [1], Ekaterina Burov[1], Hervé Montigaud [1], Rémi Lazzari [2]

[1] *Surface du Verre et Interfaces, UMR 125 CNRS/Saint-Gobain Recherche, 39 quai Lucien Lefranc, 93303 Aubervilliers Cedex, France*

[2] *Institut des NanoSciences de Paris, UMR 7588 CNRS/Sorbonne Université, 4 place Jussieu, boîte courrier 840, 75252 Paris Cedex 05, France*

[3] *Ångströmlaboratoriet, Uppsala Universitet, Polacksbackens intendentur, Box 524, 751 20, Uppsala, Sweden*

[4] *Helmholtz-Zentrum Berlin für Materialien und Energie GmbH, Albert-Einstein-Str. 15, 12489 Berlin, Germany*

Corresponding author: remi.lazzari@insp.jussieu.fr

ABSTRACT

In the context of low-emissivity glazing, the redox reaction at a buried ZnO/Ti interface is studied in model nanometer-thick film stacks synthesized by magnetron sputtering deposition. For a given amount of Ti, the roles of annealing temperature up to 550°C, of ZnO layer thickness, and of its crystalline quality are explored. The main originality of the approach is the use of hard x-ray photoemission spectroscopy to probe *in situ* chemical reactions at a buried interface in a non-destructive way. The detailed analysis of relevant core levels reveals the formation of a $Zn_xTi_yO_z$ ternary compound and the nearly complete oxidation of Ti into TiO_2. Thanks to complementary measurements of thermal desorption spectroscopy and electron probe microanalysis, unexpected diffusion of the Zn redox reaction by-product through the upper part of the stack and its desorption in vacuum are clearly evidenced. The reaction and mass transport pathways are rationalized through thermodynamic simulations.

Keywords

max 6 keywords
HAXPES, TDS, ZnO/Ti interface, magnetron sputtering

TOC

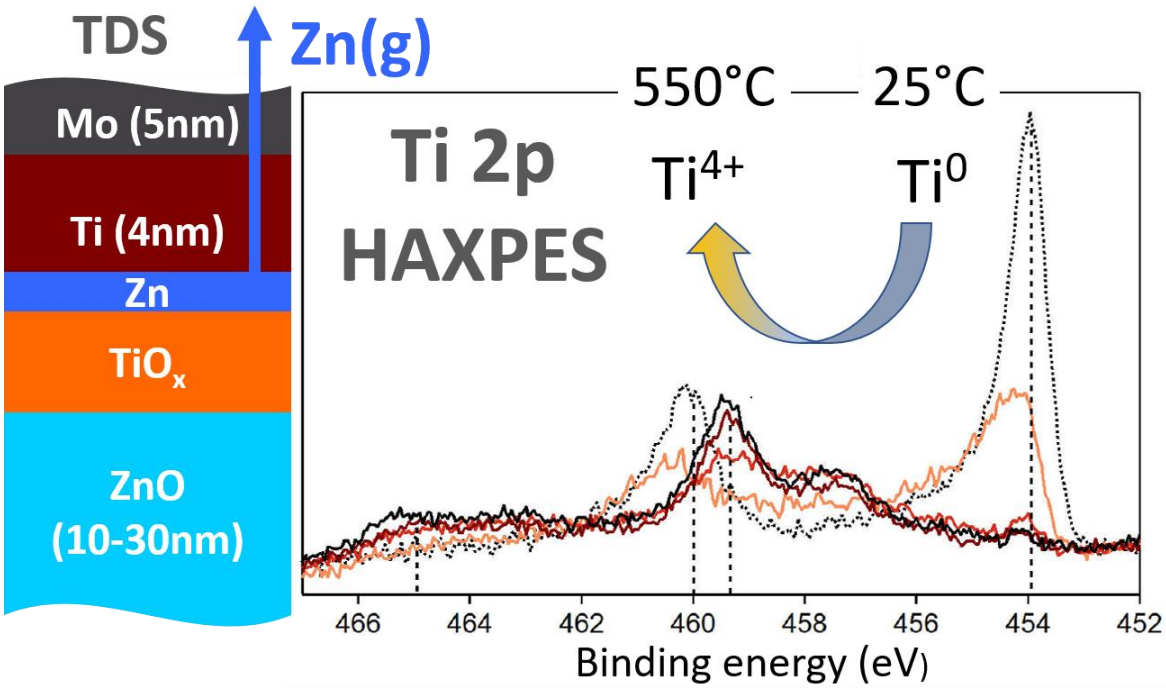

1. Introduction

Functional double glazings developed by the glass industry for thermal insulation of housing are based on complex stacks of metal and dielectric layers of nanometric thicknesses deposited onto a glass substrate. These stacks have to provide a high transparency in the visible optical range, combined with a high reflectivity at far-infrared wavelengths to minimize radiative energy losses [1]. This low-emissivity property is achieved by a *ca.* 10 nm-thick thin film of nano-crystallized Ag. This latter is embedded between two ZnO layers in order to adjust the stack optical properties, but mostly to enhance Ag crystallinity [2]. The lower the Ag film resistivity the better its infrared reflectivity. Layers are deposited by magnetron sputtering at ambient temperature as the technique, which is compatible with glass market units (3.2 x 6.0 m²), presents a high versatility in terms of materials (metal/oxide/nitride deposition) combined with large deposition rates. Quite often, the glazing, *i.e.* the glass with its thin layer stack, has to be thermally post-treated at temperatures higher than the soda-lime-silica glass transition (~550°C) in order to temper the glass panel to improve glass toughness, or to shape it for windshield applications. During this post-treatment, but also during the deposition process itself, the Ag film is exposed, either directly or through diffusion, to oxidizing species from the deposition atmosphere, the glass substrate or the closest oxide layers, which potentially worsens its electrical properties [3]. To circumvent the issue, one solution lies in the use of a very thin sacrificial and reactive layer at the Ag/ZnO interface to getter these detrimental species. Due to its high oxygen affinity and various oxidation states, Ti is one of the best candidates among transition metals [4]. A deep understanding of the chemical reaction and mass transport at the ZnO/Ti interface is thus required to optimize the performances of the functional glazing since entangled phenomena can happen in actual stacks: redox reaction, alloy formation, intermixing, diffusion, recrystallization, dewetting, etc… [5] Their respective occurrence is dictated by thermodynamics while their extent is driven by kinetics considerations, mainly diffusion and mass transport. Beyond the glazing application, this question of interface reactivity is also relevant in the control of the Schottky/ohmic characteristics of metal/oxide interfaces in opto- and nano-electronic devices [6,7].

Favored from a bulk thermodynamic point of view ($\Delta Hf = -244 kJ.mol^{-1}$ for $Ti + 2\ ZnO \rightarrow TiO_2 + 2\ Zn$ [8]), the reaction at the interface between Ti and ZnO thin films was addressed in several studies. They all showed or suspected the formation of a mixed compound at the interface and/or the appearance of metallic Zn. The reaction already occurs during the deposition of a Ti film onto ZnO even in the case of evaporated films. By using Auger Electron Spectroscopy (AES) depth profiling, Kim *et al.* observed some amount of O that diffused from ZnO into the Ti layer [9]. Borghetti *et al.* explored by X-ray Photoemission Spectroscopy (XPS) the Ti chemistry on both (0001) polar basal surfaces of ZnO single crystals (Zn- and O-terminated), during deposition and after annealing in ultra-high vacuum [10]. The authors found that deposition leads to Ti oxidation (TiO_x and a Zn-Ti-O ternary compound) with the formation of metallic Zn that ends after an equivalent thickness of *ca.* one nanometer. Beside desorption in vacuum of produced Zn, annealing revealed a face-dependent reactivity: the ZnO-O surface was more prone to react with Ti than ZnO-Zn. Already after annealing at 200°C, Ti^0 was no longer the dominant oxidation state on ZnO-O. After reaching 450°C, most of the Ti atoms were in the Ti^{4+} state. Surprisingly, the reaction between ZnO-Zn and Ti started only at 400-500°C giving rise to oxidation states of Ti higher than Ti^0. Ip *et al*. studied the effect of annealing in N_2 of a Ti/Al/Pt/Au stack deposited by e-beam on a ZnO(0001) single crystal [11]. AES profiling after annealing at 250°C showed that an interfacial reaction started between ZnO and Ti leading to the formation of Ti-O phases. After 600°C, accordingly to the authors, the ZnO-Ti contact became “completely intermixed”. Investigations concerning magnetron sputtering also highlighted an intermixing phenomenon during the deposition process itself due to the inherent high kinetic energies of the species arriving at the surface. Knut *et al*. [12] investigated stacks with Ti and ZnO thin films deposited by magnetron sputtering on Si wafers. The chemistry at the ZnO/Ti interface was probed by Hard X-ray PhotoEmission Spectroscopy (HAXPES) through a Mo protective capping layer. Prior to the successive annealing steps in vacuum, stack

characterization demonstrated that the 5 nm Ti film was already slightly oxidized, and metallic Zn was detected at the interface. After annealing at 200°C, Ti^{2+} and metallic Zn contributions increased. But astonishingly, after annealing at 350°C, while Ti oxidation further progressed, the Zn signal recovered a ZnO fingerprint. The authors assumed that metallic Zn produced by the reaction with Ti was re-oxidized by O out-diffusing from the bulk of the ZnO film. After annealing at 550°C, the whole Ti film was completely oxidized into Ti^{4+} and Zn 2p core level shift suggested the formation of a Zn_2TiO_4 compound at the interface.

In the light of previous works, this study aims at clarifying the products and the pathway of the ZnO/Ti interface reaction in thin layer stacks deposited by magnetron sputtering. To do so, the reaction was explored as a function of annealing temperature up to 550°C, ZnO film thickness and ZnO crystallinity in encapsulated stacks to compare with direct deposition experiments [9]. The puzzling behavior and outcome of Zn^0 produced by the reaction, the profile of the oxidation front and the formation of a defined interfacial compound have been revisited by combining HAXPES, Thermal Desorption Spectroscopy (TDS), Electron Probe Microanalysis (EPMA) and Time of Flight Secondary Ion Mass Spectroscopy (ToF-SIMS) in a thorough way. Thermodynamic simulations helped to rationalize the experimental findings.

2. Experimental section

2.1. Thin film deposition

The on-purpose designed samples (see Tab. 1) consisted of thin layer stacks with the following sequence (from substrate to top layer): Si/ZnO/Ti/Mo. They were deposited onto 300 µm-thick (100)-oriented Si wafers of 2'' covered by their native oxide layer. Beyond mimicking the effect of encapsulation in actual industrial stacks, the Mo layer was used to prevent Ti oxidation upon contact with the atmosphere. Its 5 nm thickness was optimized to simultaneously provide the barrier effect against the atmosphere and a sufficient transmission for the photoelectrons emitted from deeper layers. The refractory character of Mo and Ti and their poor miscibility up to high temperatures [13] (see simulated phase diagrams Fig. S8) ensured a safe annealing and a spectator behavior at this interface. Indeed, electron microscopy imaging (not shown) did not show any cracks or inhomogeneities in the Mo film surface after thermal treatments. In parallel, HAXPES evidenced only a slight deoxidation of the Mo surface upon annealing under vacuum, but no evolution of the metallic component that could testify of alloying. All the stacks were deposited by magnetron sputtering in a high vacuum chamber with a base pressure of 5×10^{-5} Pa, using Ar as working gas. The sample holder was equipped with a heating device, the temperature (up to 500°C) of which was controlled by a thermocouple placed close to the back side of the Si substrate. Due to the change of curvature from wafer to wafer, the thermal contact between the holder and the substrate led to an error of about 100°C on the achieved temperature during deposition. ZnO was deposited from a non-doped ZnO ceramic target (Neyco, purity 99.99%, 2'') activated at 40W in radio frequency (RF) mode with an Ar pressure of 0.97 Pa (gas flow: 90sccm). The substrate potential was left floating during deposition and its temperature was set either at room temperature (RT) ~25°C or at 300°C. The Ti layer was deposited at RT in direct current (DC) mode at a power of 100W from a pure metallic target (Neyco, 99.99%, 2'',) in presence of Ar at 0.36 Pa (gas flow: 30sccm). The Mo capping layer was also deposited at RT in DC mode at 150W from a pure metallic target (Neyco, 99.95% 30sccm) in presence of Ar at 0.15 Pa (gas: flow: 30sccm). The deposition rates estimated from *ex situ* thickness calibrations [14] were 0.04 $nm.s^{-1}$ for ZnO, 0.11 $nm.s^{-1}$ for Ti and 0.48 $nm.s^{-1}$ for Mo films. Reference samples involving single films of Zn, ZnO (RT / 300°C), Ti, TiO_{2-x} with or without Mo capping layers were also synthesized to help interpreting the results of the different analytical techniques. TiO_{2-x} films were obtained by adding 2% of O_2 in the gas during Ti deposition. The distance between targets and substrate was set at 120mm and, prior to any deposition, a pre-sputtering was systematically performed at least during 2 mins to clean the target.

Table 1. Thickness and deposition conditions of Si_{wafer}/ZnO/Ti/Mo samples. Thicknesses were determined by EPMA.

Sample label	ZnO deposition conditions T substrate (°C)	ZnO thickness (nm)	Ti thickness (nm)	Mo thickness (nm)
29.7@RT	Room Temperature (~25)	29.7±0.5	3.6±0.5	4.8±0.5
8.5@RT	Room Temperature (~25)	8.5±0.5	3.5±0.5	4.8±0.5
26.6@300	300 ± 100	26.6±0.5	3.7±0.5	5.1±0.5

2.2. Characterization techniques

EPMA

The EPMA were performed on a SXFive apparatus (CAMECA-AMETEK, US) to estimate the layer thicknesses of ZnO (or Zn), Ti (or TiO_2), and Mo. The electron energy applied was set at 15 keV and the current at 150 nA. Zn-Lα, Ti-Kα and Mo-Lα were the selected x-ray emission lines for quantification. Since the sample was conductive enough, no carbon overlayer was deposited to reduce charging effects. The standards used for the thickness estimation were ZnO, Mo, TiO_2. The modeling was performed using the Stratagem software (SamuX) based on the XPP model, specially adapted for stratified samples [15]. The material density values used were 10.2 for Mo, 5.6 for ZnO, 7.0 for Zn, 4.2 for TiO_2 and 4.5 g/cm³ for Ti. The quantities of Mo and Ti were found constant before and after thermal treatments at the opposite of Zn (see below).

ToF-SIMS

The ToF-SIMS depth profiles of the stacks were obtained with a TOF.SIMS-5 instrument (IONTOF, Germany). Primary ions Bi^+ accelerated at 30 keV were generated by a liquid metal ion gun (LMIG) operating in high current bunched mode with a beam current of 0.23 pA. The analyzed area was a square of 50 x 50 µm², centered in the middle of the sputtered area of 300 x 300 µm² dug by a dual source column (DSC) using Cs^+ at 2 keV with a beam current of 100 nA. Low energy (E~21 eV) electron flood gun was used in order to reduce charge effects during the acquisition in non-interlaced mode (1 s sputtering, 0.5 s pause, 2.5 s acquisition). The secondary positive ions coming from the main isotope elements M present within the layers and the substrate and their corresponding MCs^+ clusters were collected by the mass analyzer based on the time-of-flight technique. These ions provided information on the nature of the layers and their sequence in the stack as a function of sputtering time (and thus depth).

XRD

The structural properties of ZnO thin layers were studied by X-ray diffraction (XRD) using a D8 diffractometer (Bruker, Germany) with Cu Kα radiation. The acquisitions were performed in θ–2θ Bragg-Brentano configuration mode with a step of 0.030°.

HAXPES

HAXPES experiments were performed at the HIKE end-station of the KMC-1 beamline of Bessy II synchrotron (Helmholtz Zentrum Berlin). The KMC-1 beamline delivers photon energies ranging from 2 to 12 keV with an energy resolution down to 20 meV [16]. A photon energy of 4 keV was used in the present work as it provides a good compromise between intensity, energy resolution and depth sensitivity (typical inelastic mean free paths (IMFP) of ~5 nm). The take-off angle was 81-87° close to normal emission. The analyzer (Scienta R4000) pass energy was fixed at 500 eV for survey scans and at 200 eV for detailed scans of selected core levels. The sample holder was equipped with a resistive heater able to reach temperatures up to 800°C. All the acquisitions were performed at "room temperature" (at least T < 70°C), on as deposited samples and after subsequent annealing under vacuum at 250, 350, and 550°C during 10 min. The heating rate was approximately 20°C.min^{-1}. The

binding energy (BE) scale was calibrated with respect to the Au4$f_{7/2}$ core level (84.0 eV) recorded on a grounded reference gold foil electrically connected to the sample holder. With this calibration, the zero BE of the spectra corresponded to the Fermi level as measurements were free of charge effects. At a photon energy of 4 keV, using the Si(111) crystal the monochromator, the Gaussian (FWHM-G) and the Lorentzian (FWHM-L) Full Widths at Half Maximum obtained from Au 4f fit were both equal to 0.31 eV (Table 2). For quantification, all spectra were normalized by the number of scans and counting time and by the area of Mo peak, either Mo 3 $p_{3/2}$ or Mo 3 $d_{5/2}$, because the Mo quantity and its localization in the stack did not evolve between the studied samples, as deposited and after annealing. This allowed to compensate the variations from sample to sample of the photon flux and of the sample position.

TDS

TDS was performed in an ultra-high vacuum chamber equipped with a resistive heater. The set-up was composed of a quadrupole mass spectrometer (Pfeiffer, QMG 220) with a mass range of 1-200 amu enclosed in a differentially pumped quartz tube, the aperture of which was placed at a millimetric distance of the sample surface to probe only the species desorbing from the stack [17]. The temperature was estimated by a calibrated N-type thermocouple clamped on the sample holder. Temperature was linearly ramped at 0.5 °C.s^{-1} up to 600°C through a proportional-integral-derivative regulation while following selected atomic masses corresponding to desorbing species. Peaks were analyzed to determine the activation energies and order of desorption as explained below.

3. Results and discussion

3.1. Layer thickness and stack structure

The film thicknesses of the three as-deposited samples used for this study are given in Table 1. They correspond to estimates by EPMA based on the model stack sequence: Si_{wafer}/SiO_2/ZnO/Ti/Mo, *i.e.* without considering interface reaction during the deposition process. Indeed, the technique is not sensitive to the oxidation state of the probed elements.

The layered structure of the stack deposited on a Si wafer was checked by ToF-SIMS depth profiling by collecting the positive secondary ions emitted under Bi^+ sputtering and using Cs^+ for abrasion. Fig. 1 presents ToF-SIMS depth profile obtained for the 29.7@RT sample (see Table 1 for sample labels). In order to reduce artifacts due to the so-called matrix effects usually encountered with this technique, MCs^+ cluster ions of the element of interest (M) were collected: $^{133}Cs^{98}Mo^+$, $^{133}Cs^{48}Ti^+$ and $^{133}Cs^{28}Si^+$ respectively for Mo and Ti layers and Si substrate [18]. In the case of the zinc oxide layer, $^{133}Cs^{68}Zn^{16}O^+$ secondary ions were selected because (i)the main isotope $^{64}Zn^+$ of zinc presents a strong interference with $^{48}Ti^{16}O^+$ that cannot be resolved in mass events at a resolution of M/ΔM=6000 and (ii)- in order to mainly focus only on the oxide form of Zn related to ZnO layer (and not other reduced forms of Zn eventually present within the stack). According to these MCs^+ signals, the sequence of the stack Si(substrate)/ZnO/Ti/Mo was thus confirmed. Of course, the abrasion times observed for each layer do not directly follow their actual thicknesses because the sputtering rate strongly depends on the nature of the material.

The $^{133}Cs^{16}O^+$ fingerprint of oxygen is detected within the ZnO layer and at both ZnO interfaces, indicating the presence of oxide TiO_x at the interface with titanium and the native SiO_x layer at the surface of the wafer. Also, $^{133}Cs^{16}O^+$ intensity increases at the extreme surface of the Mo layer which indicates the surface oxidation of the capping layer after contact with the atmosphere.

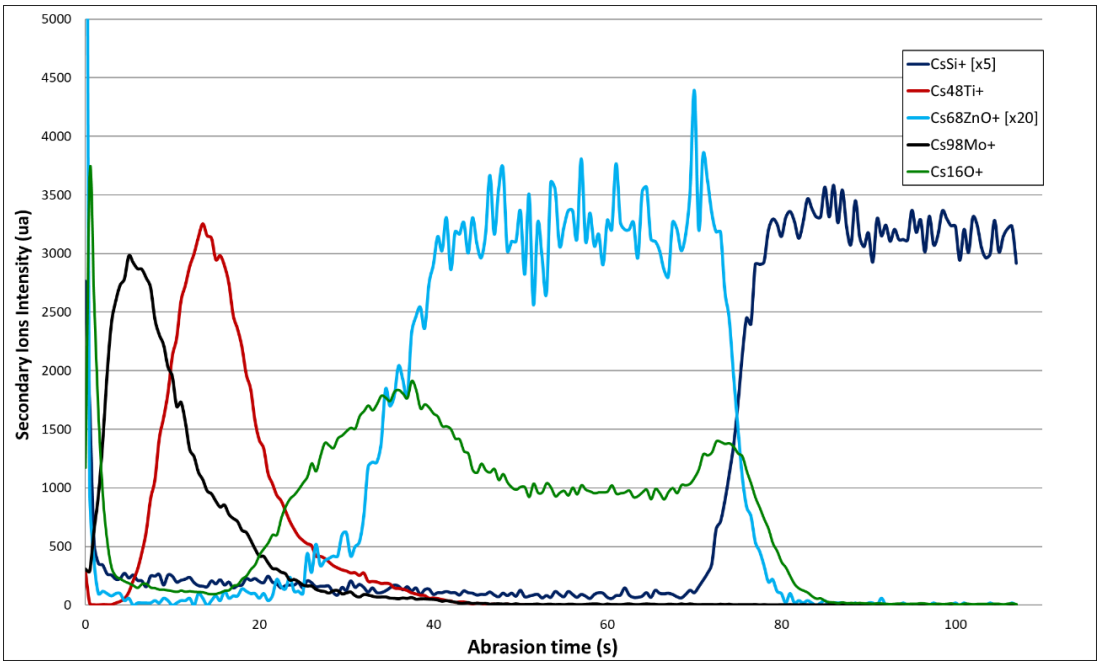

Fig. 1. ToF-SIMS depth profiles of the indicated fragments obtained for the as-deposited 29.7@RT stack. Intensities have been rescaled as indicated in the legend.

As the growth temperature is the main difference between the 29.7@RT and 26.6@300 samples, their difference in ZnO crystallinity was explored by XRD. In order to get rid of the contribution of crystallized adjacent Ti and Mo, θ–2θ scans in Bragg-Brentano configuration were acquired on simplified stacks (Si_{wafer}/ZnO) deposited in the same conditions but with slightly different thicknesses. The diffractograms demonstrate the crystallization of ZnO thin films (Fig. 2). Only two peaks corresponding to the (002) planes of the ZnO wurtzite phase (space group $P6_3mc$) are clearly identified suggesting a fiber texture along the c-[001] axis direction. As seen in Fig. 2, the ZnO(002) reflection intensity for the sample deposited at 300±100°C is approximately one order of magnitude higher than obtained at RT even though its thickness is lower (19 nm@300°C against 48 nm@RT). Furthermore, with the increase in growth temperature, the Bragg angle 2θ value shifts from 34.26° to that expected for bulk ZnO (34.43°). This suggests that the ZnO layer deposited at RT is in a higher in-plane compressive stress [19] and less crystallized and/or oriented than that grown at a higher temperature. However, the FWHM of the (002) peaks remains comparable (0.50°±0.02°) indicating that substrate temperature has no impact on the out-of-plane crystal size which Scherrer's estimate is around 16 nm.

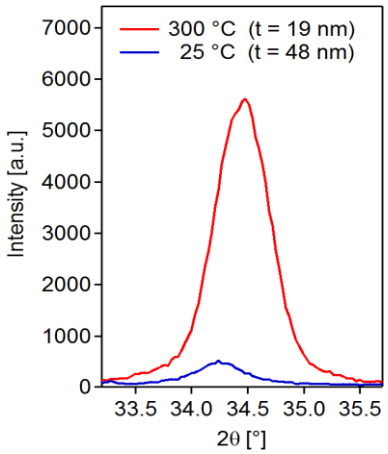

Fig. 2. Part of XRD (θ–2θ) diffractograms of ZnO thin layers deposited at room temperature, (thickness t=48nm) and at 300°C (thickness t=19nm).

HAXPES on the 29.7@RT sample

The survey HAXPES spectrum of the 29.7@RT sample, in the range of binding energies up 1300 eV (corresponding electron kinetic energies ranging from 2700 to 4000 eV) is presented in Fig. 3 with the labeling of the observed core level peaks. No trace of other elements is revealed, except for carbon (C 1*s*) which corresponds to the usual surface contamination of solids after contact with the atmosphere. In order to monitor the reaction between the ZnO and Ti layers after their deposition and during the annealing steps, a specific attention was paid to the Zn 2*p* and Ti 2*p* core levels. Peaks were fitted with the SPANCF macro of Igor Pro [20] as detailed below. All fit parameters are gathered in Table 2.

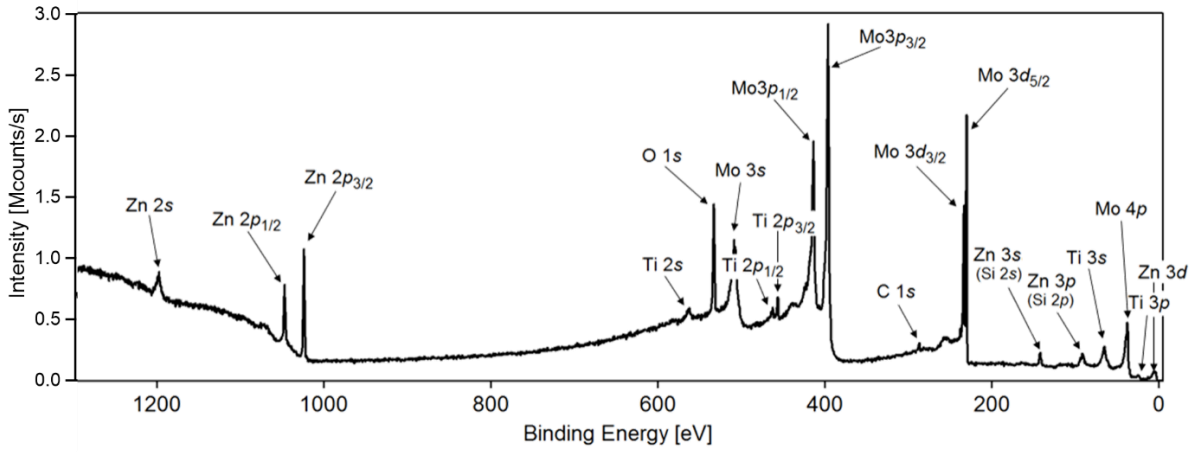

Fig. 3. HAXPES wide scan of as deposited 29.7@RT sample. Only core level peaks are visible since Auger lines are found at higher binding energies.

Table 2. Parameters used in the core level fits. Most values have been fixed from reference samples. (see text for explanation)

Core level	Ti 2p	Zn 2p $_{3/2}$	Au 4f
Binding energy shift (eV)	$E_B(Ti^{4+})$- $E_B(Ti^{0+})$ = 4.8 $E_B(Ti^{4+})$-$E_B(Ti^{3+})$ = 1.6 $E_B(Ti^{3+})$-$E_B(Ti^{2+})$ = 1.6	E_B(ZnO) = 1021.9 E_B(ZnO)-$E_B(Zn^0)$ = 0.3 $E_B(Zn_xTi_yO_z)$-E_B(ZnO) = 0.3	84
Spin-orbit splitting (eV)	$\Delta E_B(Ti^0)$ = 6.1 $\Delta E_B(Ti^{2+}, Ti^{3+}, Ti^{4+})$ = 5.8	--	3.7
Branching ratio	0.5 ± 0.01	--	0.66
FWHM-L (eV)	$\sigma(Ti^{n+}\ 2p_{3/2})$ = 0.39 $\sigma(Ti^0\ 2p_{3/2})$ 1.28 $\sigma(Ti^{n+}\ 2p_{1/2})$ = 0.78	0.49	0.31
FWHM-G (eV)	$\sigma(Ti^{n+}\ 2p_{3/2})$ = $\sigma(Ti^{n+}\ 2p_{1/2})$ = fitted > σ(Au 4f)	fitted	0.31
PCI asymmetry of metallic state	$\gamma(Ti^0\ 2p_{1/2})$ = 0.38 $\gamma(Ti^0\ 2p_{3/2})$ = 0.60	$\gamma(Zn^0\ 2p_{3/2})$ = 0.12	--

Ti 2*p* core level analysis

The BE corresponding to the Ti 2*p* spin-orbit split doublet is in between those of Mo 3*s* and Mo 3*p* core levels. Consequently, the shape of Ti 2*p* core level is influenced by the background related to the nearby Mo 3*p* peak located at lower BE. A spectrum acquired on a sample without Ti showed that the background in this region of interest is close to a straight line (**Fig. S1a**). Therefore, prior to Ti 2*p* analysis a linear background, which slope corresponds to the average of the linear baselines at lower and higher BE sides of the Ti 2*p* doublet, was systematically subtracted (**Fig. S1b**). Aside from a Shirley active background [21, 22], the fit of Ti 2*p* core level included all possible oxidation states of Ti (Ti^0, Ti^{2+}, Ti^{3+}, and Ti^{4+}). The components were modeled by a convolution of a Gaussian function G(x) with (i) a Lorentzian one L(x) for oxidized Ti^{n+} or (ii) a so-called Post-Collision Interaction (PCI) function [23] to describe the typical asymmetry of Ti^0 metal core level. The gaussian profile is assigned to instrumental broadening (such as the energy profile of the x-ray excitation, thermal broadening, response function of the analyzer) and distribution of core level shifts. The latter is assigned to fluctuations of the chemical environment of the elements. The lorentzian and PCI profiles describe, respectively, the lifetime of the core hole, a contribution from the excitation, and the typical asymmetry found in metal core level due to electron-hole excitations. Thus, the fitting protocol involved 4 doublets which each component had 5 parameters: peak position, peak area, Gaussian and Lorentzian broadening (FWHM-G and FWHM-L) and peak asymmetry. In front of the total of 40 fit parameters, constraints were applied based on values found in the literature [8, 24] and our own analysis of reference samples (**Fig. S2**) of metallic Ti and TiO_2 films deposited directly on Si wafer for which the native SiO_2 prevents any interfacial reaction. In order to account for possible band bending effects, the position of Ti^0 $2p_{3/2}$ with respect to Ti^{2+} $2p_{3/2}$, Ti^{3+} $2p_{3/2}$, and Ti^{4+} $2p_{3/2}$ peaks was let free. But BE shifts between the Ti^{2+}/Ti^{3+} and Ti^{3+}/Ti^{4+} components were kept fixed at 1.6 eV, directly inspired by the numerous values proposed in the literature and our own references samples [4, 8, 12, 24]. Similarly, the spin-orbit splitting of the Ti^0 2*p* doublet was fixed at 6.1 eV and that of Ti^{2+}, Ti^{3+}, and Ti^{4+} oxide Ti 2*p* components at 5.8 eV [4, 8, 12, 24]. The FWHM-L of Ti $2p_{3/2}$ was set to 0.39 eV, for all oxidation states, in agreement with the Ti 2*p* fit results for the references while it is was set at 0.78 and 1.28 eV for Ti^0 and all oxide Ti $2p_{1/2}$ components (**Fig. S1**). The difference of broadening between the two components of the doublet is due to complex many-body effects as detailed in Ref. [25]. The Gaussian contribution was let free for all peaks but common to both components Ti $2p_{1/2}$ and Ti $2p_{3/2}$ of the same doublet. It varies between different fits, but it is not less than 0.35 eV which corresponds to the experimental resolution. The PCI-asymmetry parameter was fixed at 0.60 for Ti^0 $2p_{3/2}$ and at 0.38 for the Ti^0 $2p_{1/2}$ as obtained from fits of references. In other words, the asymmetric line profile of metallic samples is used as a template for fit of actual samples. Similar results could have been obtained with other asymmetric shapes. At last, the branching ratio *i.e.* the relative areas of the Ti 2*p* doublet components was chosen close to the theoretical value for a *2p* level *i.e.* 0.5±0.01 and in agreement with databases [25b,25c]

Fig. 4 shows the Ti 2*p* spectrum obtained for 29.7@RT sample just after deposition and after subsequent annealing at 250, 350 and 550°C during 10 min under vacuum. The previously described fitting protocol was applied to each spectrum and the different identified components are shown on the graphs. A sizable transformation of Ti chemical state occurs upon annealing. Similarly, to the observation of Knut *et al.* for sputter deposited layers [12], the reaction between the ZnO and Ti layers already starts at the deposition stage even at RT. The spectrum is mainly represented by an asymmetric doublet at 454.05 eV and 460.15 eV corresponding to Ti^0 $2p_{3/2}$ and Ti^0 $2p_{1/2}$ separated by a spin-orbit splitting of 6.1 eV. Nevertheless, small contributions of Ti^{2+} and Ti^{4+} are already present. After annealing at 250°C, the Ti^0 component intensity decreases giving rise to growing oxidized Ti^{n+} states. After 350°C, all the oxidized Ti components are present within a broad peak with an intensity maximum at 459.0 eV corresponding to the Ti^{4+} feature. After annealing at 550°C, the Ti film is almost transformed into Ti^{4+}, except for a tiny Ti^{3+} residual component.

Zn 2p core level analysis

Due to the large spin-orbit splitting of the Zn 2p level (23 eV) [8] which is well beyond any possible chemical shift, the Zn chemical environment was scrutinized using only Zn $2p_{3/2}$ core level peak position and shape. Zinc can adopt two oxidation states (Zn^{2+} and Zn^0) that can be clearly distinguished via their LMM Auger profiles [26]. Unfortunately, their low kinetic energy (~988 eV) does not provide a large enough electron mean free path for their detection from the present stacks. According to literature [8, 27, 28, 29], the chemical shift of Zn $2p_{3/2}$ between the metallic asymmetric Zn component and the ZnO symmetric one is quite small c.a. 0.3±0.1 eV. Furthermore, as argued by Knut *et al.* [12], a $Zn_xTi_yO_z$ mixed oxide could also be formed upon annealing giving rise to a symmetric peak at a slightly different BE. Unfortunately, no BE data on the expected spinel Zn_2TiO_4 compound is available in the literature and the only values of Zn $2p_{3/2}$ BE shift relative to the ZnO component for Zn-based mixed oxides are: -0.2 eV for Zn_2AlO_4 [30], +0.3 eV for Zn_2SiO_4, and -0.9 eV for $ZnFe_2O_4$ [31]. Thus, the Zn $2p_{3/2}$ peak was fitted with three components assigned to metallic Zn^0, ZnO, and mixed compound ($Zn_xTi_yO_z$). The ZnO and $Zn_xTi_yO_z$ peaks were taken as symmetric FWHM functions while the Zn^0 related peak was fitted with the convolution of a Gaussian and an asymmetric PCI function. Similarly to Ti *2p* core level analysis, reference samples of pure Zn and ZnO deposited directly on the Si wafer helped fixing some parameters (Fig. S3). While the FWHM-G were let free for all components, the FWHM-L was fixed at 0.49 eV for all the peaks and the asymmetry of the Zn-related PCI peak at 0.12. If the BE shift of the ZnO component with respect to the Zn metallic one was set at 0.3 eV, the relative shift of the $Zn_xTi_yO_z$ component was determined and fixed at 0.3 eV (relative to ZnO one) from the Zn $2p_{3/2}$ fit obtained with the sample annealed at 550°C (see below). At last, the background was accounted for similarly to Ti *2p*.

Fig. 4e-h gather the results of such Zn $2p_{3/2}$ spectra analysis before and after annealing. Spectra are also overlapped in Fig. S4 to highlight the line shape evolution. For the as-deposited sample, the major ZnO component is accompanied by a minor contribution of metallic Zn which can be assigned to the ZnO/Ti reaction occurring from the early beginning of the Ti deposition [12]. The IMFP of the Zn 2*p* electrons excited at a photon energy of 4 keV (kinetic energy of ~ 2980 eV) in ZnO is $\lambda_{Zn2p}^{ZnO} = 4.7$ nm [32], corresponding to a probing depth of ~14 nm, not speaking about signal damping in the upper Ti and Mo layers. Thus, the Zn $2p_{3/2}$ spectra represent the upper part of the ZnO layer and the metallic contribution obviously comes from the ZnO/Ti interface. After annealing at 250°C, the ZnO-related intensity diminishes at the expense of the metallic Zn one and the signal becomes more asymmetric. After 350°C, the peak symmetry is recovered and the ZnO component is again the major contribution. Finally, after 550°C, the peak shifts towards higher binding energies leading to the emergence of the $Zn_xTi_yO_z$ component.

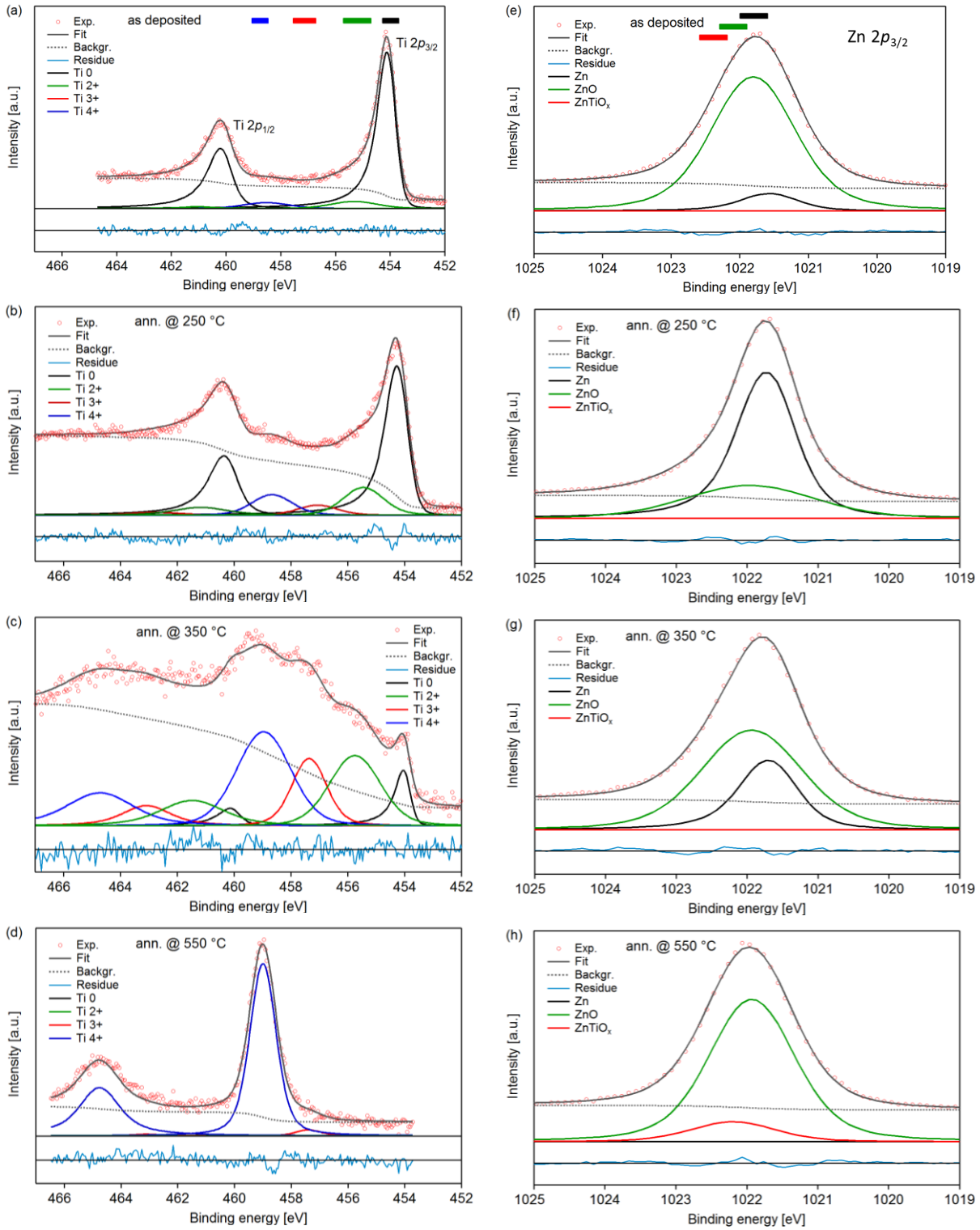

Fig. 4. (a-d) Ti 2*p* doublet and (e-f) Zn $2p_{3/2}$ HAXPES spectra and the corresponding peak fitting for the 29.7@RT sample in (a)(e) the as-deposited state and after annealing under high vacuum at (b)(f) 250°C, (c)(g) 350°C and (d)(h) 550°C. Colored rectangles on top of the graphs (a) and (e) point to reference Ti $2p_{3/2}$ and Zn $2p_{3/2}$ peak positions found in literature (see text): Ti^0 (black), Ti^{2+} (green), Ti^{3+} (red), Ti^{4+} (blue) and Zn- (black), ZnO- (green), $Zn_xTi_yO_z$ -related (red). Data (red circles), fit (continuous grey line), background (dotted black line), residue (light blue line) are overlapped with all components using the same color code.

Chemical evolution from peak areas and the loss of Zn

Based on the areas of the different Ti 2*p* and Zn $2p_{3/2}$ contributions, the proportion of the different oxidation states and compounds for Ti and Zn can be estimated. Assuming that, on the one hand, the Ti^{n+} species are distributed homogeneously within the layer and considering that, on the other hand, the photo-ionization cross-section and the apparatus response for the Ti *2p* level are the same, the area fractions are directly proportional to the corresponding atomic concentrations from which an average oxidation state can be determined. The same analysis was applied to Zn $2p_{3/2}$ core level.

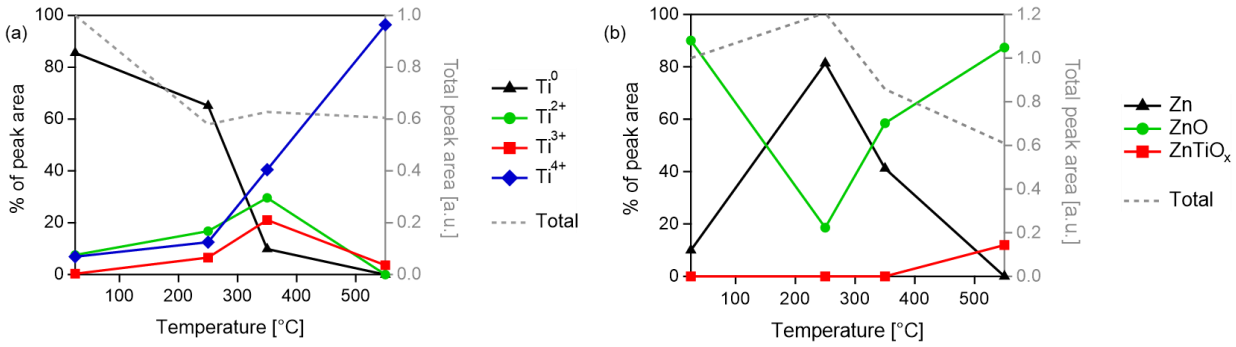

Fig. 5. Evolution of the 29.7@RT sample after annealing under high vacuum: (a) fractions (left scale) of each Ti^0, Ti^{2+}, Ti^{3+} and Ti^{4+} components with respect to the total Ti 2*p* peak area (right scale). (b) Fractions (left scale) of Zn^0, Zn^{2+}(ZnO) and Zn^{2+}($Zn_xTi_yO_z$) with respect to the total Zn $2p_{3/2}$ peak area (right scale). Absolute detected intensities are normalized to the as-deposited state, the Mo signal being used as a reference.

Fig. 5 presents the evolution of these area fractions as a function of annealing in parallel to the Ti *2p*/ Zn $2p_{3/2}$ absolute total peak which is proportional to the whole detected quantity of Ti and Zn. Remind that all intensities are renormalized to Mo signal to correct for inherent variations from measurement to measurement. The evolution of Ti 2*p* spectra with annealing conveys a gradual oxidation of the Ti film from a metallic (Ti^0) to fully oxidized (Ti^{4+}) state and a reduction of ZnO. In an as-deposited film, the ZnO component dominates. It then collapses after the annealing step at 250°C and transforms into a metallic state. However, the increase of the absolute Zn $2p_{3/2}$ intensity and the decrease of that of Ti 2*p* (dotted lines in Fig. 5) points at diffusion of the produced metallic Zn towards the upper part of the stack. It is confirmed by the further disappearance of the Zn metal signal after annealing at 350°C. This evolution suggests a loss of Zn. The decrease of probed Zn amount continues after annealing at 550°C while the intensity of Ti 2*p* remains constant as also demonstrated through the EPMA analysis. The proportion of the different contributions derived from core levels also evolves to a nearly pure Ti^{4+} form via intermediate oxidation states for titanium and a full oxidized form for zinc dominated by ZnO, but also with the final formation of a $Zn_xTi_yO_z$ compound.

The loss of Zn after the different annealing steps under vacuum was confirmed *a posteriori* by EPMA. Assuming a pure ZnO layer in the analysis, its thickness decreased from 29.7 nm to 21.0 nm. Considering the reaction 2 ZnO + Ti ➔ TiO_2 + 2 Zn and the bulk densities of Ti and ZnO (4.5 and 5.6 g/cm^3 respectively), the consumption of the whole 3.6 nm Ti layer leads to a reduction of 9.4 nm of the ZnO layer thickness which is comparable to the 8.7 nm loss experimentally observed here. Furthermore, a reference stack with a ZnO layer of similar thickness (16 nm) but without the Ti layer presented no significant thickness change (< 0.5nm) upon annealing at 550°C. Therefore, the observed decrease of ZnO layer thickness clearly follows the balance of the above chemical reaction between ZnO and Ti. Moreover, mass conservation shows that the Ti-rich film thickens from $t_{Ti} = 3.8$ nm (pure Ti) to $t_{TiO2} = 6.3$ nm (assuming only pure TiO_2) while the remaining ZnO underneath still behaves as a bulk material on a photoemission point of view with a thickness more than three times the IMFP

($\lambda_{Zn2p}^{ZnO} = 4.7$ nm [32]). Accounting for similar IMFPs of $\lambda_{Zn2p}^{TiO2} = \lambda_{Zn2p}^{Ti} = 5$ nm in both materials [32], the expected decrease of Zn $2p_{3/2}$ absolute intensity upon full annealing:

$$\frac{I(Zn\ 2p3/2\ \ annealed)}{I(Zn\ 2p3/2\ as{-}deposited)} = \exp\left[-\left(\frac{t_{TiO2}}{\lambda_{Zn2p}^{TiO2}} - \frac{t_{Ti}}{\lambda_{Zn2p}^{Ti}}\right)\right] = 0.6$$

agrees with the experimental finding (grey dotted line in Fig. 5-b). Regarding Ti 2p absolute area evolution (grey dotted line Fig. 5-a), a continuous decay is observed upon annealing as expected theoretically from a simple transformation of Ti into TiO_2 and film thickening:

$$\frac{I(Ti\ 2p\ annealed)}{I(Ti\ 2p\ as{-}deposited)} = \frac{\varrho_{TiO2}\lambda_{Ti2p}^{TiO2}\left[1-\exp\left(-\frac{t_{TiO2}}{\lambda_{Ti2p}^{TiO2}}\right)\right]}{\varrho_{Ti}\lambda_{Ti2p}^{Ti}\left[1-\exp\left(-\frac{t_{Ti}}{\lambda_{Ti2p}^{Ti}}\right)\right]} = 0.8. \qquad \varrho_{TiO2} = 0.0533\ mol.cm^{-3}, \qquad \varrho_{Ti} =$$

$0.0942\ mol.cm^{-3}$ are the Ti concentration in the bulk materials and $\lambda_{Ti2p}^{TiO2} = 5.8$ nm, $\lambda_{Ti2p}^{Ti} = 5.9$ nm the corresponding IMFPs. Nevertheless, one should keep in mind that such quantitative analyses ignore any potential gradient of oxidation and the presence of a $Zn_xTi_yO_z$ compound.

HAXPES background shape analysis

The background of the Zn 2*p* doublet (Fig. 6a) also provides noteworthy information confirming the mechanism of Zn diffusion. After annealing at 250-350°C, the Zn 2*p* background at higher binding energies exhibits a different trend compared to the other spectra. S. Tougaard showed that this shape critically depends on the in-depth distribution of the probed element [34, 35]. As an example, Fig. 6b is an adaptation from Ref. [34] showing the shape of the XPS background of the Cu 2*p* doublet as a function of the position of Cu in Au: (i) placed on top of Au, (ii) homogeneously distributed in volume, (iii) buried in a form of a thin layer, and (iv) situated underneath Au in a "bulk"-like form. By comparing with the present findings for the 29.7@RT sample, it appears that for the as-deposited sample, the background profile corresponds to case (iv) of Fig. 6b, and the change of the Zn 2*p* background after annealing at 250°C corresponds to a part of Zn atoms that are either localized in the pre-surface region as a thin layer (case (iii) in Fig. 6b), or on the sample surface (case (i) in Fig. 6b). Indeed, according to thermodynamic data (Fig. S10), Zn and Ti [36] can form defined compounds at 250°C while Zn and Mo [37] appear immiscible (Fig. S9). Therefore, during annealing at 250°C, Zn can alloy with Ti diffuse through it and Mo before sublimating at the stack surface. The desorption from the surface which is favored by the already high Zn vapor pressure at 300°C (~ 10^{-5} mbar compared to the vacuum level of 10^{-9} mbar [38]) will be fully confirmed later by TDS (see Sect. 3.5).

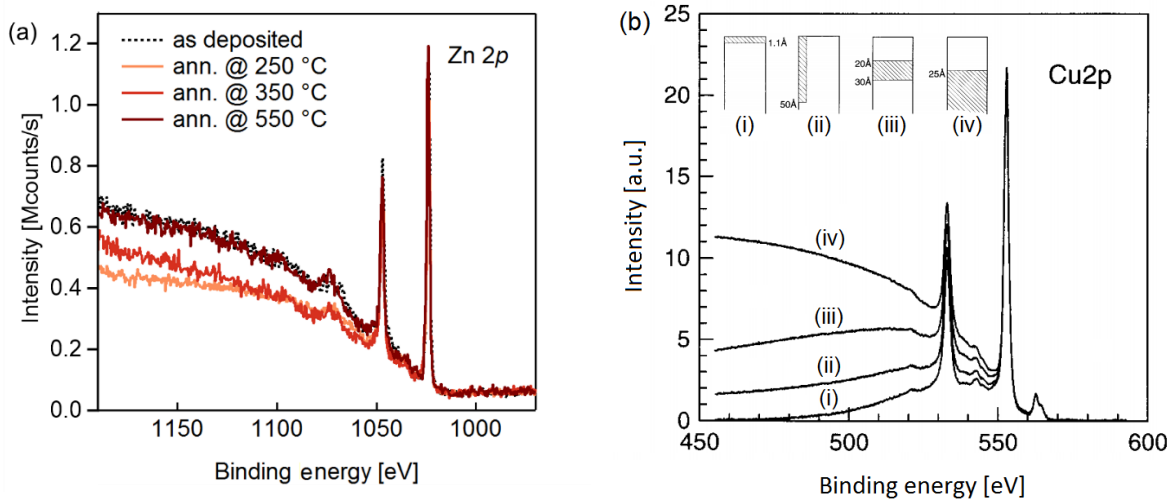

Fig. 6. (a) Evolution of Zn 2*p* core level background as a function of the annealing steps. (b) Background of the Cu 2*p* doublet as a function of the position of Cu in Au: (i) placed on top of Au, (ii)

distributed in volume, (iii) buried in a form of a thin layer, and (iv) located underneath Au in a "bulk"-like form. Adapted from Ref. [34].

3.2. Impact of ZnO thickness: HAXPES of the 8.5@RT sample

The effect of the ZnO thickness on Ti oxidation was tackled with a similar stack but with a thinner ZnO film (8.5 nm instead of 29.7 nm) following the same analysis protocol as the 29.7@RT sample (Table 1). Fig. 7 shows the Ti 2*p* and Zn 2$p_{3/2}$spectra right after the stack deposition and after a similar annealing sequence.

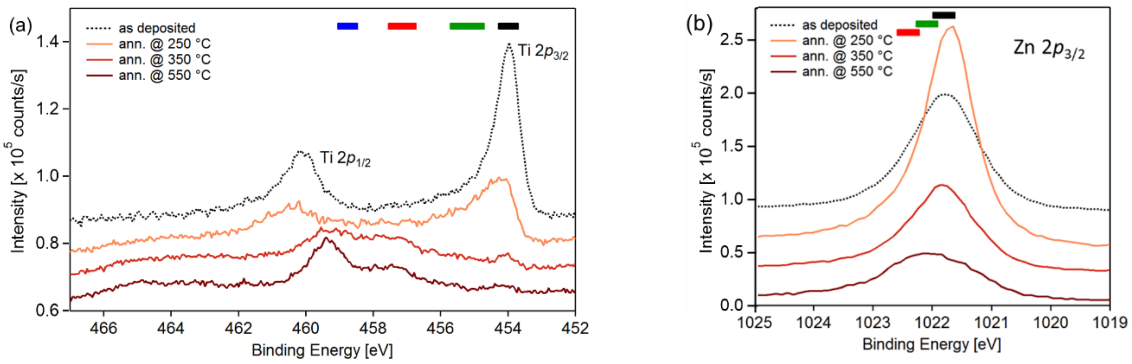

Fig. 7. HAXPES spectra of 8.5@RT sample obtained for as deposited sample and after subsequent annealing under high vacuum at 250°C, 350°C and 550°C: (a) Ti 2*p* and (b) Zn 2$p_{3/2}$. Colored rectangles on top of the graphs correspond to reference peak positions found in literature: (a) Ti^0 (black), Ti^{2+} (green), Ti^{3+} (red), Ti^{4+} (blue) components for Ti 2$p_{3/2}$, and (b) Zn- (black), ZnO- (green), $Zn_xTi_yO_z$-related (red) components for Zn 2$p_{3/2}$.

The same fitting protocol (not shown) was applied to both series of Ti 2*p* and Zn 2$p_{3/2}$ spectra with the same assumptions and constraints as in the case of the 29.7@RT sample. The outcome in terms of the relative amount of each of the Ti 2$p_{3/2}$ and Zn 2$p_{3/2}$ contributions is reported in Fig. 8 in addition to the total peak areas corresponding to the quantity of Ti and Zn detected by HAXPES.

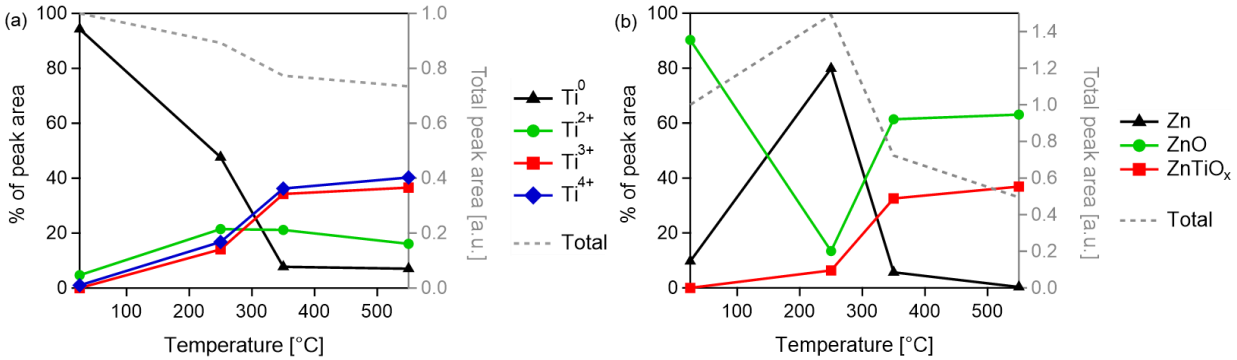

Fig. 8. Evolution of composition of the 8.5@RT sample upon high vacuum annealing. Same legend as Fig. 5.

Up to 250°C, Ti 2*p* spectrum evolves in a similar way as for the 29.7@RT sample (Fig. 5a); the dominant contribution is the metallic one (Ti^0). Above that temperature, the Ti^0 component becomes less intense and higher oxidation states appear in the spectrum as a growing shoulder (Fig.7a). After 350°C, oxidized states of Ti prevail over Ti^0, with Ti^{4+} becoming the most intense component. But, after annealing at 550°C, in contrast to the 29.7@RT sample, the spectrum does not evolve much; aside from a slightly larger Ti^{4+} signal, the two other oxidation states remain sizable (Fig. 8a). Neither an extra

annealing step at 550°C nor at 650°C (not shown) do result in a full conversion into Ti^{4+}. Regarding Zn $2p_{3/2}$ spectra (Fig.7b), the scenario is similar to that of 29.7@RT although the evolution of the peak shape and position is more pronounced here with a thinner ZnO layer. The fractions of the Zn, ZnO, and $Zn_xTi_yO_z$ components poorly evolve after annealing at 350°C (Fig. 8b), even after extra annealing at 650°C (not shown).

As in the case of the 29.7@RT sample, the total Ti 2*p* intensity decays after annealing at 250°C and in parallel, the Zn 2*p* one shows a maximum. After annealing at 550°C the Ti-based film is largely under-oxidized (average oxidation state of 3.04 against 3.96 for 29.7@RT), with 7% of Ti being still in the metallic state Ti^0 and only 41% of Ti^{4+}. The lack of evolution at higher temperatures demonstrates that the reaction between ZnO and Ti could not progress further. As in the case of 29.7@RT, one can link the changes of the peak intensity and shape to the creation of metallic Zn which moves towards the top of the sample during annealing at 250°C. Again, Zn starts leaving the stack between 250 and 350°C. In turn, the shift of the peak position towards higher binding energies reveals the formation of a $Zn_xTi_yO_z$ compound after annealing at 550°C. The departure of Zn is also confirmed *a posteriori* by EPMA as the remaining EPMA thickness is 0.5 nm against 8.5 nm before annealing (see Table 1). Since 9.4 nm can be indeed considered as a minimal thickness of ZnO required to oxidize the whole 3.5 nm Ti film, the reaction in the 8.5@RT sample does not end by a complete oxidation of Ti due to the lack of ZnO reactant. The remaining zinc is involved in ZnO (60%) and $Zn_xTi_yO_z$ (40%) phases. Contrary to the 29.7@RT sample, the corresponding Zn $2p_{3/2}$ signal is not simply that of a thick ZnO layer damped by a TiO_2-rich layer. Its change amounts to:

$$\frac{I(Zn\ 2p3/2\ annealed)}{I(Zn\ 2p3/2\ as-deposited)} = \frac{\varrho_{Zn-rich}\lambda_{Zn2p}^{Zn-rich}\left[1-\exp\left(-\frac{t_{Zn-rich}}{\lambda_{Zn2p}^{Zn-rich}}\right)\right]}{\varrho_{ZnO}\lambda_{Zn2p}^{ZnO}\exp\left[-\frac{t_{Ti}}{\lambda_{Zn2p}^{Ti}}\right]} = 0.2 \text{ with } \varrho_{Zn-rich} \approx (0.6 * \varrho_{ZnO} + 0.4 * 2\varrho_{Zn2TiO4}) = 0.0577\ mol.cm^{-3},\ \varrho_{ZnO} = 0.0672\ mol.cm^{-3},\ \varrho_{Zn2TiO4} = 0.0217\ mol.cm^{-3},$$

$t_{Zn-rich} = \frac{t_{ZnO}^{EPMA}\varrho_{ZnO}}{\varrho_{Zn-rich}} = 0.6$ nm and if one assumes similar IMFPs in $Zn_xTi_yO_z$ and ZnO. Although lower than the experimental finding (0.5; grey dotted line in Fig. 8b), this value is well within the uncertainty of EPMA thickness determination ($\Delta t_{ZnO}^{EPMA} = 0.5$ nm) and model assumptions.

3.3. Impact of the ZnO crystallinity: HAXPES of the 26.6@300 sample

The XRD characterization of the 29.7@RT and 26.6@300 samples (see Sect 3.1) suggested that the ZnO film grown at an elevated temperature has a better crystallinity. In order to study its impact on the reaction between ZnO and Ti, similar sequences of annealing and HAXPES analyses were applied to the 26.6@300 sample. The Ti 2*p* and Zn $2p_{3/2}$spectra obtained for the as-deposited sample and after annealing at 350°C and 550°C are presented in Fig. 9 while the results of quantification from core levels are shown in Fig. 10.

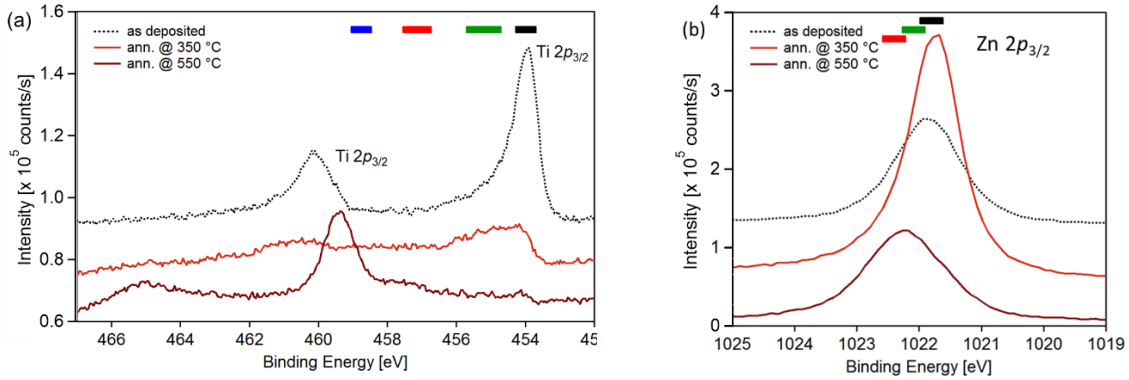

Fig. 9. Evolution of HAXPES spectra of 26.6@300 sample after high vacuum annealing. Same legend as Fig. 7.

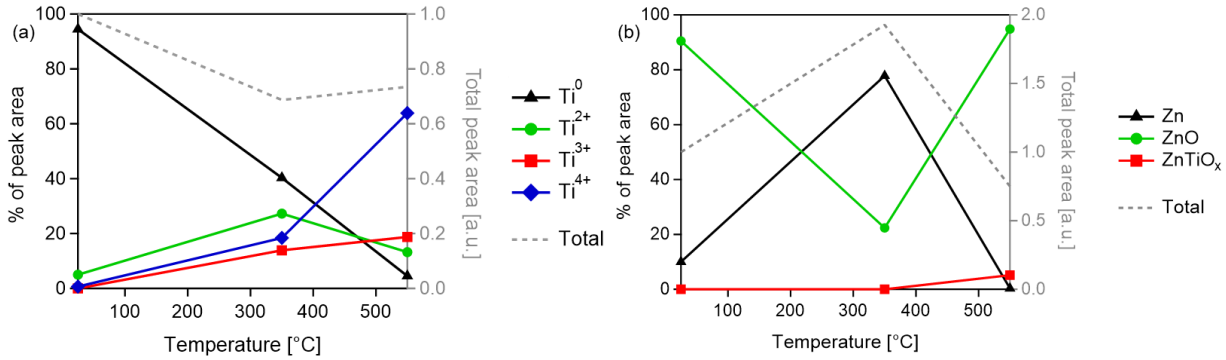

Fig. 10. Evolution of composition of the 26.6@300 sample upon high vacuum annealing. Same legend as Fig. 5.

The as-deposited Ti film is mainly metallic but after its annealing at 350°C, in contrast with the case of the 29.7@RT sample, the Ti^0 component still dominates the spectrum (Fig. 9a). After 550°C, Ti^{4+} becomes the major component but nevertheless, lower oxidation states are still visible. The average oxidation state of Ti after annealing at 550°C is 3.37, with 4% of Ti^0 and only 64% of Ti^{4+} within the film. Concerning the Zn $2p_{3/2}$ spectrum of the as-deposited sample, ZnO is already slightly reduced. After annealing at 350°C, the Zn $2p_{3/2}$ peak becomes more intense and asymmetric due to the major contribution of the metallic form of Zn. After 550°C, the Zn $2p_{3/2}$ peak intensity drops and its symmetric shape is recovered. Furthermore, like in the case of 29.7@RT, the peak shifts towards higher binding energies, due to the contribution of Zn^{2+}($Zn_xTi_yO_z$).

Even if the sample was not analyzed by HAXPES after annealing at 250°C, it appears that the better crystallinity of the ZnO film leads to a shift of the threshold of Ti oxidation to temperatures higher than 350°C. Furthermore, although the quantity of ZnO is sufficient for a full reaction (26.6 nm compared to the theoretical minimum of 9.4 nm), the average oxidation state of Ti after the final annealing at 550°C is significantly reduced (3.37) compared to that obtained for the 29.7@RT sample (3.96). Considering Zn $2p_{3/2}$ and Ti $2p$ absolute intensities, the same formation of metallic Zn at 350°C followed by its migration upwards in the stack is found. Final values at 550°C are similar to those of the 29.7@RT sample. At 550°C, the metallic Zn contribution disappears from the Zn $2p_{3/2}$ spectrum, and a mixed $Zn_xTi_yO_z$ compound is formed. An *a posteriori,* EPMA measurement confirms the reduction of the ZnO layer thickness after the whole annealing sequence; the estimated final thickness is 17.0 nm which represents an equivalent ZnO loss of 9.6 nm. This value is close to that expected from the chemical reaction (9.4nm). Within the accuracy (0.5 nm) of the analysis, no significant difference on the mass loss, related to the improved quality of ZnO (better crystallization and stoichiometry), is observed compared to the first two samples with ZnO layers deposited at RT.

3.4. Thermal Desorption Spectroscopy of the 29.7@RT and 26.6@300 samples

Previous HAXPES and EPMA results suggested the formation of metallic Zn during the annealing at 250°C and its diffusion to the upper layers of the stack during the next annealing steps before its desorption under vacuum. In order to confirm this scenario and to determine the exact temperature of occurrence of the phenomena in a much more accurate way than with the previous 100°C stepwise measurements, both the 29.7@RT and 26.6@300 samples were analyzed by TDS (Fig. 11a). In both cases, the samples were heated up to 600°C at a rate of 0.5°C/s under vacuum. The following mass/charge (m/q) ratios of interest corresponding to the indicated fragments were recorded: 2 ($^1H_2^+$), 16 ($^{16}O_2^{2+}$, $^{16}O^+$), 18 ($^1H_2{}^{16}O^+$), 28 ($^{12}C^{16}O^+$, $^{14}N_2^+$), 48 ($^{48}Ti^+$), 64 ($^{64}Zn^+$, $^{48}Ti^{16}O^+$), 66 ($^{66}Zn^+$), 80 ($^{64}Zn^{16}O^+$, $^{48}Ti^{16}O_2^+$), 98 ($^{98}Mo^+$).

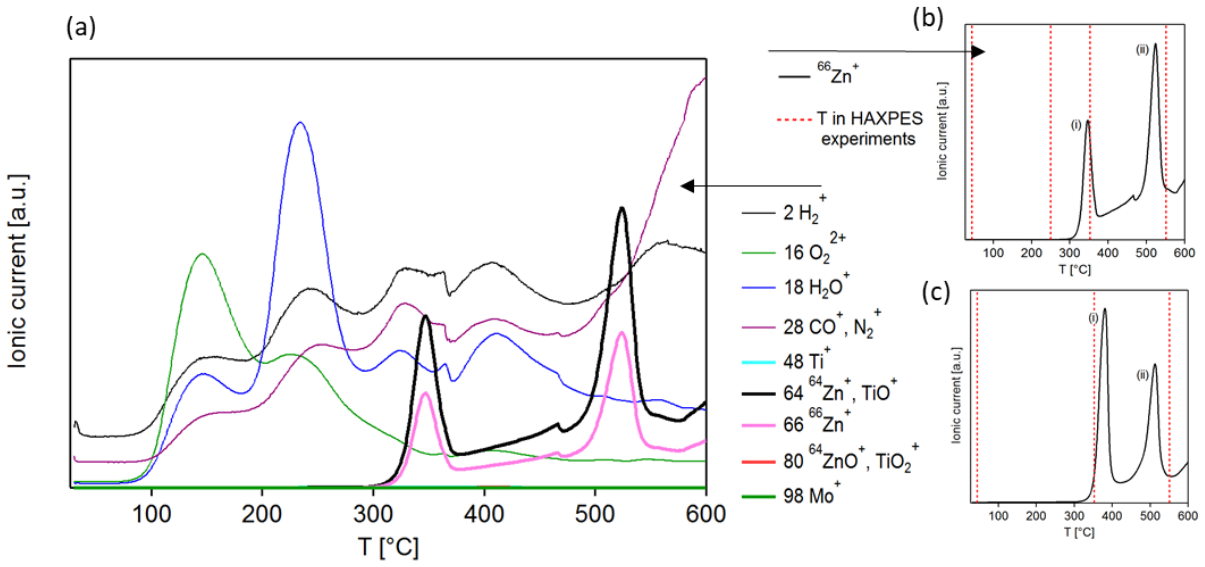

Fig. 11.(a) TDS signals versus temperature for mass/charge ratios of m/q=2 ($^1H_2^+$), 16 ($^{16}O^+$), 18 ($^1H_2{}^{16}O^+$), 28 ($^{12}C^{16}O^+$, $^{14}N_2^+$), 48 ($^{48}Ti^+$), 64 ($^{64}Zn^+$, $^{48}Ti^{16}O^+$), 66 ($^{66}Zn^+$), 80 ($^{64}Zn^{16}O^+$, $^{48}Ti^{16}O_2^+$), 98 ($^{98}Mo^+$) of 29.7@RT sample. $^{66}Zn^+$ TDS signal (b) of the 29.7@RT sample and (c) of the 26.6@300 sample. In Fig (b) and (c), dotted vertical bars correspond to the annealing temperature in the HAXPES studies *i.e.* as deposited, at 250, 350 and 550°C.

Spurious intense H_2, H_2O and CO desorption peaks attributed to the surface contamination due to the atmosphere exposure are detected around 150°C, 250°C and higher temperatures (Fig. 11a). They are accompanied by a reduction of Mo oxides (not shown) but, in agreement with its refractory character, the Mo capping layer does not desorb at such low temperatures [see $^{98}Mo^+$ (m/q=98)]. Nevertheless, Zn desorption is clearly visible in the signals m/q=64 and 66 related to the two main zinc isotopes ^{64}Zn and ^{66}Zn; since their ratio of intensities matches their relative abundance (48%/64%), any contribution of $^{48}Ti^{16}O^+$ to m/q=64 can be ruled out all the more than no Ti desorption is observed [see $^{48}Ti^+$ (m/q=48); $^{48}Ti^{16}O_2^+$ (m/q=80) signals]. Moreover, the lack of $^{64}Zn^{16}O^+$ (m/q=80) demonstrates that Zn desorbs as monoatomic species.

Figs.11b-c (where the annealing temperatures applied during HAXPES measurements are reported as red vertical dotted lines) compare the evolution of the $^{66}Zn^+$ desorption signal of the 29.7@RT and 26.6@300 samples. In both cases, two desorption peaks are clearly observed, the first one (i) shifting from 350°C to 380°C and the second one (ii) from 525°C to 515°C when depositing the ZnO film at higher temperature. A desorption threshold analysis in the framework of Polyani-Wigner [39] model as detailed in Ref. [40, 17, 41] was applied to all desorption peaks to obtain the corresponding desorption order (n) and activation energies (E_a) of the limiting step. Shortly, this approach consists in finding the best n value that linearizes the desorption peak as a function of the inverse of temperature at the peak threshold. In a short range of temperature, the characteristic frequency (ν), n, and E_a can be assumed to be constant and independent of the quantity of matter that had poorly changed. The E_a values estimated by this approach are respectively 1.75 and 2.43 eV for peaks (i) and (ii) of the 29.7@RT sample and 2.37 and 2.31 eV for those of the 26.6@300 one. Moreover, n=0 desorption order was found for all peaks except for the first one (i) of the 26.6@300 sample which is better described by an order n=1.5–2.0.

In order to verify if the desorption of Zn produced by the ZnO/Ti interface reaction is limited by the reaction kinetic itself or by the diffusion through the different layers above, four additional samples were analyzed by TDS. Spectra are shown in supporting materials. The corresponding stacks and conclusions for these reference samples are as follows:

- Si wafer / ZnO (15.9 nm) / Mo (4.5 nm): Zn desorption is absent (not shown) thus confirming that ZnO films by themselves are thermally stable and do not decompose upon annealing at temperatures up to 600°C; a similar conclusion was reached by the EPMA thickness analysis;
- Si wafer / Zn (1.3 nm) / Mo (3.0 nm): Zn desorption through Mo starts at around 200°C and continues at higher temperatures (Fig. S5a);
- Si wafer / Zn (1.6 nm) / Ti (3.3 nm) / Mo (3.0 nm): the first peak of Zn desorption through Ti is situated around 350°C, and two more desorption peaks are observed at 450 and 550°C (Fig. S5b);
- Si wafer / Zn (1.8 nm) / TiO_x (4.0 nm) / Mo (3.0 nm): Zn desorption through a TiO_x film deposited under O_2 atmosphere is observed between 450 and 550°C (Fig. S5c).

Furthermore, Mouchaal *et al.* [42] observed Zn desorption in the case of a 1.1 nm thick Ti layer evaporated on the two polar (0001) surfaces of ZnO single crystals; for those experiments, the question of diffusion through upper layers is irrelevant. For both orientations, Zn desorption was observed around 520°C [peak (ii)] but only deposits on O-terminated surface led to a feature at lower temperature [220°C; peak (i)]. They also noted that when the Ti thickness was reduced to sub-monolayer level (<0.4 nm), the first desorption peak (i) shifted to higher temperature (320°C) and the high temperature peak (ii) was quenched.

Based on all these observations, one can conclude that the peak (ii) around 520°C is intrinsic to the barrier of reaction between ZnO and Ti; it does not shift or disappear when changing the nature of ZnO and the capping layer (uncapped single-crystal *vs* capped thin polycrystalline film), the surface termination in case of free surface (ZnO-O *vs* ZnO-Zn) or the crystallization state (deposition at RT *vs* at 300°C). It is not hampered by Zn diffusion through neither Mo nor Ti that happens at much lower temperatures. Being of order zero order, it is not limited by the available amount of Zn. However, the temperature of peak (ii) matches with that of the desorption of Zn through TiO_x (Fig. S5c). Thus, its activation energy is characteristic of the barrier of ZnO/Ti reaction at film interface and likely involves contributions from reactants diffusion to the interface and from diffusion of the produced Zn through the formed oxidized Ti layers.

On the other hand, peak (i) is absent for single crystals, except for the sub-monolayer deposit that can react readily with surface defects (such as hydroxyl groups) during deposition [10]. In stacks, a likely hypothesis is that Zn is already available at the moment of desorption (or produced just before it) due to reaction with the ZnO layer. Its desorption [peak (i)] is limited only by the Zn diffusion through the upper Ti layer, which becomes possible only above ~ 350°C, according to Fig. S5b. However, the slowdown of the process is likely due to the progressive formation of a TiO_x barrier for Zn diffusion at the ZnO/Ti interface. The zero-desorption order of peak (i) of 29.7@RT sample (in agreement with that of the Si/Zn/Ti/Mo sample) means that the desorption rate is not limited by the available amount of Zn. This hypothesis is supported by HAXPES results after annealing at 250°C that reveal the presence of Zn in metallic form in the stack in agreement with TDS (Fig. 11a). At last, both E_a and n related to peaks (i) are larger for the 26.6@300 sample than for the 29.7@RT one demonstrating an impact of the crystallinity of the ZnO film on the formation of the TiO_x diffusion barrier.

3.5. Thermodynamic simulations for Zn-Ti-O ternary system and scenario of reaction/diffusion during annealing under high vacuum

In order to rationalize the HAXPES, TDS and EPMA observations and due to the absence of literature data concerning the Zn-Ti-O ternary phase diagram at reduced pressure, thermodynamic simulations using the *FactSage* software were performed [43]. These thermochemical calculations are based on the minimization of the Gibbs energy, to find the most stable phases at different chemical potentials and compositions. However, being based on a homogeneous mixture of the pure elements, these simulations do not consider neither the layered structure of the present systems nor the kinetics of reaction and diffusion. The phases and compounds taken into account were the followings: (i) solids: ZnO, TiO_2 (rutile), TiO, Ti_2O_3, Zn_2TiO_4, Zn, Ti, $TiZn_x$ defined compounds (x=15, 10, 5, 3, 2, 1, 0.5) and solid solution $ZnO(TiO_2)_x$, (ii) liquids: Zn, Ti, $(ZnO)_x(TiO_2)_y$ and (iii) gases: Zn, O_2. Mo was not considered since, beyond surface oxide decomposition at 250°C, its HAXPES signal and therefore its metallic character

did not evolve. First, the Zn-Ti-O ternary diagram was established at atmospheric pressure. The extracted binary diagrams, such as Ti-Zn (Fig. S6a) or ZnO-TiO_2 (Fig. S7a) were in close agreement with those respectively proposed by Vassilev *et al.* (Fig. S6b) [44], Yang *et al.* (Fig. S7b) [45] and Dulin *et al.* [46] except for the eutectic temperatures and the lack of $ZnTiO_3$ and $Zn_2Ti_3O_8$ phases and of other polymorphs of TiO_2. Due to the absence of experimental thermodynamic data, these two Zn-Ti-O compounds are not proposed by *FactSage.* However, this should not impact the present conclusion as their formation was mainly reported for TiO_2 proportions higher than in the present study (see Fig. S7b). Based on this comparison showing the soundness of the *FactSage* approach, simulations were then carried out at a pressure of 10^{-7}Pa corresponding to the HAXPES and TDS experiments. The ZnO-Ti binary diagram at low molar fraction of Ti (Fig.12) was computed from 0 to 0.35 Ti/(Ti + ZnO) mol/mol because it represents the interface of interest. The following phases can be formed: Zn(s), Zn(g), O_2(g) TiO_2(rutile) and Zn_2TiO_4 (s), in addition to the solid solution $ZnO(TiO_2)_x$. The vertical dotted line at 0.33 corresponding to the integrated composition of Ti(3.5nm)/ZnO(9.4nm) should represent the thermodynamic pathway of the homogeneous mixture followed upon annealing. The main outcome of this simulation is the possibility to obtain Zn(g) above 100°C from Zn(s) in equilibrium with oxides and, above all, to form a non-stoichiometric solid solution $ZnO(TiO_2)_x$ and a defined compound Zn_2TiO_4 which can decompose into Zn(g) and TiO_2 at 580°C. These temperatures poorly depend on the Ti fraction in a large domain of composition.

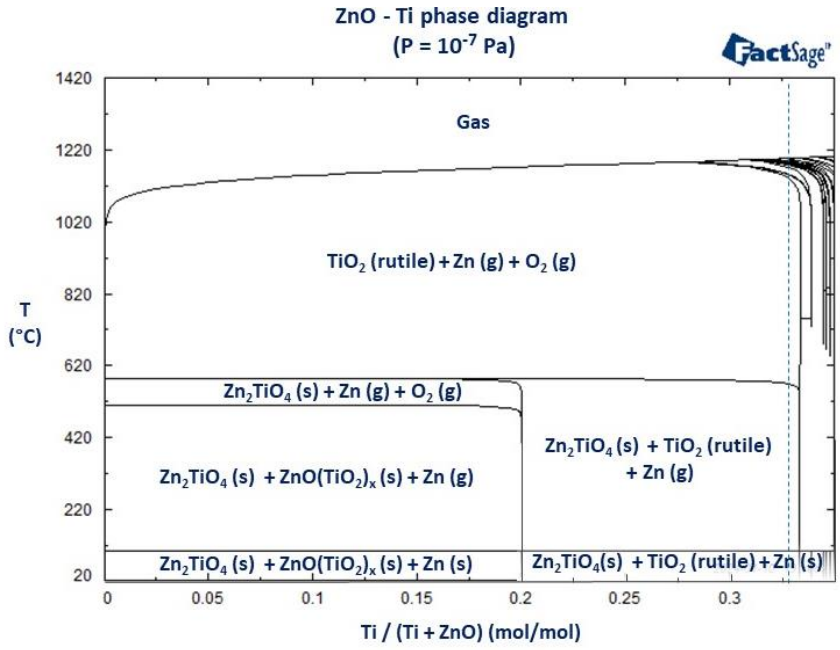

Fig. 12. ZnO-Ti phase diagram simulated by *FactSage* software at 10^{-7} Pa. The vertical dotted blue line corresponds to the molar fraction of 33% of Ti corresponding to film thicknesses ZnO(9.5 nm)/Ti(3.4 nm). The indexes (s) and (g) stands for solid and gaz phase.

These insights allow us to propose a scenario for the reaction/diffusion phenomena occurring in the stratified ZnO/Ti system from RT up to 550°C. It is schematically illustrated in Fig.13. In agreement with the strong negative enthalpy of reaction [8] and with the calculated phase diagram (Fig. 12), the ZnO-Ti interface is thermodynamically not stable at all temperatures. As a consequence of the PVD deposition process, a thin TiO_x film and some amount of Zn metal are initially present at the interface between ZnO and Ti films. While heating up to 250°C, Ti/TiO_x continue to reduce the upper part of the ZnO layer, leading to a thickening of the TiO_x layer and the formation of further Zn metal. Limited by the diffusion through metallic Ti (Fig. S5b) and/or by the formation of $TiZn_x$ compounds as expected from the simulated Ti-Zn phase diagram [43] (Fig. S10), Zn metal stays below/inside the Ti film until the next temperature step at ~350°C. Then it diffuses through the remaining Ti layer (Fig. S5b) and the

Mo capping (Fig. S5a) before desorbing [peak (i) in TDS]. Metallic Zn which is further produced by the reaction, and possibly by the decomposition of the $ZnO(TiO_2)_x$ solid solution which is expected around 510°C (Fig. 12), is encapsulated under TiO_x and certainly TiO_2 which release it around ~500°C [peak (ii) in TDS, Fig. S5c]. Zn desorption explains the disappearance of Zn^0 fingerprint in photoemission (performed after annealing at 550°C) which was previously misinterpreted as a reoxidation phenomenon induced by diffusion of O from bulk of ZnO [12]. After this final annealing at 550°C, titanium is mainly involved in TiO_2 and a minority $Zn_xTi_yO_z$ compound detected in photoemission is formed, probably at the ZnO/TiO_x interface. The final temperature is borderline for a full decomposition of Zn_2TiO_4 into TiO_2 which is expected around 580°C (Fig. 12). At last, the Ti film is fully oxidized if the ZnO layer is thick enough (ZnO ~ 9.4 nm for Ti ~3.5nm).

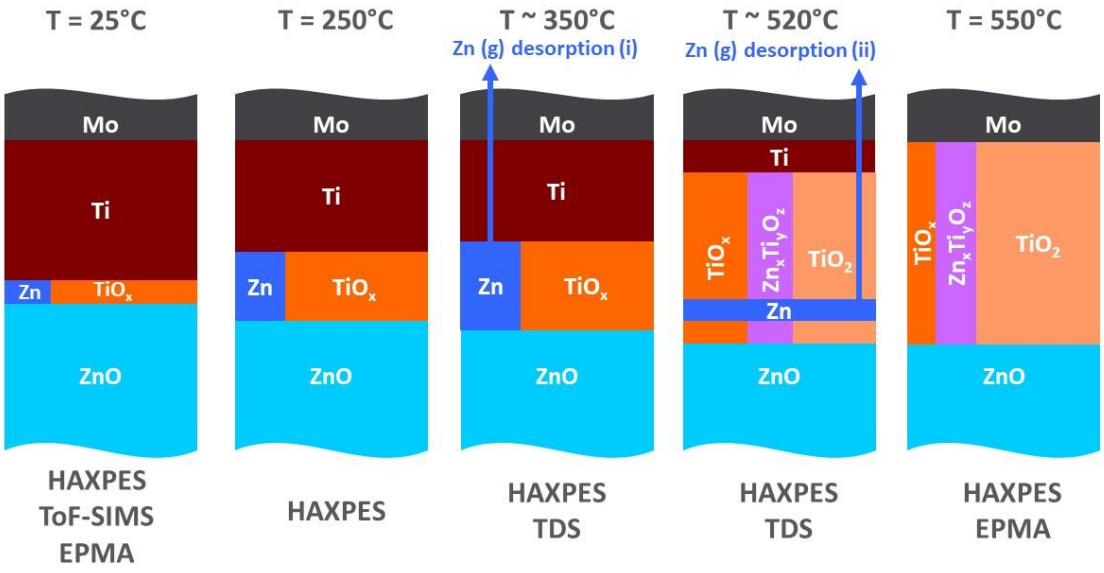

Fig. 13. Schematic reaction/diffusion mechanisms between layers at different temperatures as proposed from experiments and thermodynamic simulations.

4. Conclusions

The redox behavior of encapsulated nanometer-thick sputtered layers of ZnO and Ti was explored during annealing under high vacuum. The interfacial reaction leading to the formation of new compounds was monitored by a combination of HAXPES, TDS and EPMA and rationalized by thermodynamic simulations. Thanks to its capability to probe buried interfaces in a non-destructive way, HAXPES allowed an *in situ* follow-up of the evolution of the chemical states of the layers up to 550°C. First, the Ti + ZnO redox reaction already starts during the early stage of the Ti deposition. It proceeds progressively with the intermediate formation of TiO_x, metallic Zn and a $Zn_xTi_yO_z$ compound (potentially Zn_2TiO_4) before ending by the nearly complete oxidation of Ti in TiO_2 at 550°C. As evidenced by HAXPES and demonstrated by TDS, Zn diffuse from the reaction front up to the top of the stack before desorbing. TDS evidenced two Zn desorption peaks, the one at lower temperature (350°C) being hindered by the diffusion through Ti and that at higher temperature (520°C) being intrinsic to the barrier of reaction and diffusion at $ZnO/TiO_x/Ti$. The reactivity of this interface appears to be dependent on the ZnO crystallization; the better ZnO is crystallized, the higher the temperature of its reduction by Ti. This work illustrated the complexity of oxido-reduction reaction and diffusion

processes happening in low-E glazing upon annealing and the potentialities of HAXPES to follow phenomena in realistic samples.

Acknowledgements
The authors gratefully acknowledge the support of the Helmholtz-Zentrum Berlin for supplying synchrotron radiation beamtime at beamline KMC-1 of BESSY II, Thierry Cretin for the ToF-SIMS depth profiling and his help for the interpretations of the signals, and the EMC2 department of SGR Paris for EPMA. The PhD thesis of E. C. was funded by Saint-Gobain Research Paris (Aubervilliers, France) and Agence Nationale de la Recherche et de la Technologie.

[1] C.G. Granqvist. Solar energy materials. *Advanced Materials*, 15:1789–1803, 2003.
[2] M. Arbab. The base layer effect on the dc conductivity and structure of direct current magnetron sputtered thin films of silver. *Thin Solid Films*, 381:15–21, 2001.
[3] R.C. Ross. Observations on humidity-induced degradation of ag-based low-emissivity films. *Solar Energy Materials*, 21:25–42, 1990.
[4] T. Godfroid, R. Gouttebaron, J. P. Dauchot, Ph Leclère, R. Lazzaroni, and M. Hecq. Growth of ultrathin Ti films deposited on SnO_2 by magnetron sputtering. *Thin Solid Films*, 437:57–62, 2003.
[5] Q. Fu, T. Wagner, S. Olliges, and H.-D. Carstanjen. Metal-oxide interfacial reactions: Encapsulation of Pd on TiO_2(110). *J. Phys. Chem. B*, 109(2):944–951, jan 2005.
[6] E. V. Monakhov, A. Y. Kuznetsov, and B. G. Svensson. Zinc oxide: bulk growth, role of hydrogen and Schottky diodes. *J. Phys. D: Appl. Phys.*, 42(15):153001, 2009.
[7] L. J. Brillson and Y. Lu. Zno Schottky barriers and ohmic contacts. *J. Appl. Phys.*, 109(12):121301, 2011.
[8] NIST X-ray photoelectron spectroscopy database. https://srdata.nist.gov/xps/Default.aspx, 2012.
[9] K.-K. Kim, S.-H. Han, T.-Y. Seong, and W.-K. Choi. Low-resistance Ti/Au ohmic contacts to Al-doped ZnO layers. *Applied Physics Letters*, 77:1647–1649, 2000.
[10] P. Borghetti, Y. Mouchaal, Z. Dai, S. Chenot, R. Lazzari, and J. Jupille. Orientation-dependent band-bending and chemistry for Ti on polar ZnO surfaces. *Phys. Chem. Chem. Phys.*, 19:10350–10357, 2017.
[11] K. Ip, M. E. Overberg, Y. W. Heo, D. P. Norton, S. J. Pearton, C. E. Stutz, B. Luo, F. Ren, D. C. Look, and J. M. Zavada. Hydogen incorporation and diffusivity in plasma-exposed bulk ZnO. *Appl. Phys. Lett.*, 82:385–387, 2003.
[12] R. Knut, R. Lindblad, S. Grachev, J. Y. Faou, M. Gorgoi, H. Rensmo, E. Søndergård, and O. Karis. Reactive ZnO/Ti/ZnO interfaces studied by hard x-ray photoelectron spectroscopy. *J. Appl. Phys.*, 115:043714, 2014.
[13] J. M. Dupouy and B. L. Averbach, atomic arrangements in titanium and molybdenum solid solutions, *Acta Metallurgica*, 9: 755-763, 1961
[14] I. Gozhyk, L. Dai, Q. Hérault, R. Lazzari, and S. Grachev. Plasma emission correction in reflectivity spectroscopy during sputtering deposition. *J. Phys. D: Appl. Phys.*, 52:095202, 2018.
[15] J. L. Pouchou and F. Pichoir. Electron Probe X-Ray Microanalysis Applied to Thin Surface Films and Stratified Specimens. *Scanning Microscopy*, 7:167-189, 1993.
[16] M. Gorgoi, S. Svensson, F. Schäfers, G. Öhrwall, M. Mertin, P. Bressler, O Karis, H. Siegbahn, A. Sandell, H. Rensmo, W. Doherty, C. Jung, W. Braun, and W. Eberhardt. The high kinetic energy photoelectron spectroscopy facility at BESSY : progress and first results. *Nucl. Instrum. Methods A*, 601:48–53, 2009.
[17] H.-L. Thi Le, R. Lazzari, J. Goniakowski, R. Cavallotti, S. Chenot, C. Noguera, J. Jupille, A. Koltsov, and J.-M. Mataigne. Tuning adhesion at metal/oxide interfaces by surface hydroxylation. *J. Phys. Chem. C*, 121:11464–11471, 2017.
[18] H. Gnaser. Improved quantification in secondary-ion mass spectrometry detecting MCs^+ molecular ions. *Journal of Vacuum Science & Technology A*, 12:452–456, 1994.

[19] J. Hinze and K. Ellmer. In situ measurement of mechanical stress in polycrystalline zinc-oxide thin films prepared by magnetron sputtering. *Journal of Applied Physics*, 88:2443–2450, 2000.
[20] E. Kukk. Spectrum analysis by curve fitting (spancf) - macro package for igor pro. http://www.geocities.ws/ekukk/intro.htm.
[21] D.A. Shirley. High-resolution X-ray photoemission spectrum of valence bands of gold. *Phys. Rev. B*, 5:4709–4714, 1972.
[22] A. Herrera-Gomez, M. Bravo-Sanchez, O. Ceballos-Sanchez, and M. O. Vazquez-Lepe. Practical methods for background subtraction in photoemission spectra. *Surf. Interface Anal.*, 46:897–905, 2014.
[23] P. Van der Straten, R. Morgenstern, and A. Niehaus. Angular dependent post-collision interaction in Auger processes. *Zeitschrift für Physik D Atoms, Molecules and Clusters*, 8(1):35–45, 1988.
[24] M. C. Biesinger, L. W. M. Lau, A. R. Gerson, and R. St.C. Smart. Resolving surface chemical states in XPS analysis of first row transition metals, oxides and hydroxides: Sc, Ti, V, Cu and Zn. *Applied Surface Science*, 257:887–898, 2010.
[25] P. S. Bagus, C. J. Nelin, C. R. Brundle, and S. A. Chambers. A new mechanism for XPS line broadening: The 2p-XPS of Ti(iv). *The Journal of Physical Chemistry C*, 123:7705–7716, 2019.
[25b] J. Scofield, Theoretical photoionization cross sections from 1 to 1500 keV, Technical Report UCRL-51326, Lawrence Livermore Laboratory, 1973
[25c] M. Trzhaskovskaya and V. Yarzhemsky, Dirac-Fock photoionization parameters for HAXPES applications, Atom. Data Nucl. Data, 119, 99-174, 2018[26] J. H. Fox, J. D. Nuttall, and T. E. Gallon. Solid state effects in the Auger spectrum of zinc and oxidized zinc. *Surf. Sci.*, 63:390–402, 1977.
[27] J. C. Klein and D. M. Hercules. Surface characterization of model Urushibara catalysts. *Journal of Catalysis*, 82:424–441, 1983.
[28] . S. Wehner, P. N. Mercer, and G. Apai. Interaction of H_2 and CO with $Rh_4(CO)_12$ supported on ZnO. *Journal of Catalysis*, 84:244–247, 1983.
[29] G. Deroubaix and P. Marcus. X-ray photoelectron spectroscopy analysis of copper and zinc oxides and sulphides. *Surface and Interface Analysis*, 18:39–46, 1992.
[30] B. R. Strohmeier. Zinc aluminate ($ZnAl_2O_4$) by XPS. *Surface Science Spectra*, 3:128–134, 1994.
[31] L. S. Dake, D. R. Baer, and J. M. Zachara. Auger parameter measurements of zinc compounds relevant to zinc transport in the environment. *Surface and Interface Analysis*, 14:71–75, 1989.
[32] S. Tougaard. QUASES-IMFP-TPP2M Software. http://www.quases.com/products/quases-imfp-tpp2m/.
[33] E. Chernysheva. *Zinc oxide growth and its interfaces with metals observed by photoemission*. PhD thesis, University Pierre and Marie Curie, France, 2017.
[34] S. Tougaard. Quantitative XPS: non-destructive analysis of surface nano-structures. *Appl Surf Sci*, 100-101:1–10, 1996.
[35] S. Tougaard. Improved XPS analysis by visual inspection of the survey spectrum. *Surf Interface Anal*, 50:657–666, 2018.
[36] J. L. Murray. The Ti-Zn (titanium-zinc) system. *Bulletin of Alloy Phase Diagrams*, 5:52–56, 1984.
[37] V. Raghavan. Al-Mo-Zn (aluminum-molybdenum-zinc). *Journal of Phase Equilibria and Diffusion*, 30:630, 2009.
[38] Vapor pressure calculator: https://www.iap.tuwien.ac.at/.
[39] H. Ibach. *Physics of Surfaces and Interfaces*, volume 10. Springer-Verlag Berlin Heidelberg, 2006.
[40] A. M. De Jong and J. .W. Niemantsverdriet. Themal desorption analysis: comparative test of ten commonly applied procedures. *Surf. Sci.*, 233:355–365, 1990.
[41] M. Messaykeh, S. Chenot, P. David, G. Cabailh, J. Jupille, A. Koltsov, and R. Lazzari. An in situ and real-time plasmonic approach of seed/adhesion layers: chromium buffer effect at the zinc/alumina interface. *Crystal Growth & Design*, 21:3528–3539, 2021.

[42] Y. Mouchaal. *Elaboration et étude de nouvelles électrodes transparentes substituts de l'ITO dans les dispositifs optolectroniques*. PhD thesis, Oran 1 University, Algeria, 2016.
[43] C. W. Bale, P. Chartrand, S. A. Degterov, G. Eriksson, K. Hack, R. Ben Mahfoud, J. Melan con, A. D. Pelton, and S. Petersen. FactSage thermochemical software and databases. *Çalphad*, 26:189–228, 2002.
[44] G. P. Vassilev, X. J. Liu, and K. Ishida. Reaction kinetics and phase diagram studies in the Ti–Zn system. *Journal of Alloys and Compounds*, 375:162–170, 2004.
[45] J. Yang and H. H. Swisher. The phase stability of $Zn_2Ti_3O_8$. *Materials Characterization*, 37:153–159, 1996.
[46] F. H. Dublin and D. E. Rase. Phase equilibria in the system ZnO-TiO_2. *Journal of the American Ceramic Society*, 43:125–131, 1960.